

Configurable Artificial Spin Ice with Site-Specific Local Magnetic Fields

Vineeth Mohanan Parakkat¹, Gavin M. Macauley², Robert L. Stamps³, and Kannan M. Krishnan^{1,*}¹Department of Materials Science and Engineering, 323 Roberts Hall, University of Washington, Seattle, Washington 98195, USA²SUPA, School of Physics and Astronomy, University of Glasgow, Glasgow G12 8QQ, United Kingdom³Department of Physics and Astronomy, University of Manitoba, Winnipeg, Manitoba R3T 2N2, Canada (Received 18 June 2020; accepted 18 December 2020; published 7 January 2021)

We demonstrate ground state tunability for a hybrid artificial spin ice composed of Fe nanomagnets which are subject to site-specific exchange-bias fields, applied in integer multiples of the lattice along one sublattice of the classic square artificial spin ice. By varying this period, three distinct magnetic textures are identified: a striped ferromagnetic phase; an antiferromagnetic phase attainable through an external field protocol alone; and an unconventional ground state with magnetically charged pairs embedded in an antiferromagnetic matrix. Monte Carlo simulations support the results of field protocols and demonstrate that the pinning tunes relaxation timescales and their critical behavior.

DOI: 10.1103/PhysRevLett.126.017203

Artificial spin ice (ASI) [1–3] are two-dimensional arrays of magnetostatically interacting nanomagnets that act as giant Ising spins. When arranged on specific lattices, they mimic the frustrated interactions [4] found in naturally occurring pyrochlore crystals [5,6]. These two-dimensional artificial magnetic systems [7–12], made possible by developments in lithography [13], allow exploration of structures that are difficult or impossible to realize with chemically synthesized compounds. ASI is also a promising prototype for investigating emergent phenomena such as magnetic monopoles [14–16], Coulomb phases [15], and spin fragmentation [10,14,17,18]. Recently, ASI has been proposed for data storage and computational applications [19–22], offering device options which integrate memory with active logic.

Most previous studies on ASI have dealt with understanding the collective behavior of arrays of *identical* nanomagnets, with an emphasis on different lattice geometries in order to utilize the anisotropic features of the dipolar field [1,9,10,18,19,23–26]. There is growing interest in designing reconfigurable arrays in which the desired magnetic configurations can be “written” by applying local magnetic fields using magnetic probes either with [12] or without [19] the help of global magnetic fields. These include attempts to access specific moment configurations in ASI, either by field protocols [27] or by modifying individual nanomagnets [28]; however, these are restricted to a small number of nanomagnetic building blocks. In this Letter, we demonstrate a way to alter the properties of individual nanomagnets, in such a way that it affects their relaxational dynamics. This allows configurability of the global behavior of the lattice and provides a way to engineer a preferred magnetic texture.

Earlier [29], we demonstrated how exchange bias [30,31] can be applied as a global field (in the device

reference frame using an antiferromagnetic IrMn layer) on a square ASI composed of Fe nanomagnets. This allowed us to tune and rearrange the vertex energy levels of the array as a whole. Enabled by this result but extending the lithography to the second level (see Supplemental Material [32], Sec. I), we restrict the exchange bias to a truly *local* field and study its effects when applied on the *x* sublattice of the canonical square ASI geometry with different periodicities [integer multiples p of the lattice constant a ($=400$ nm) as in Figs. 1(a) and 1(b)]. We term

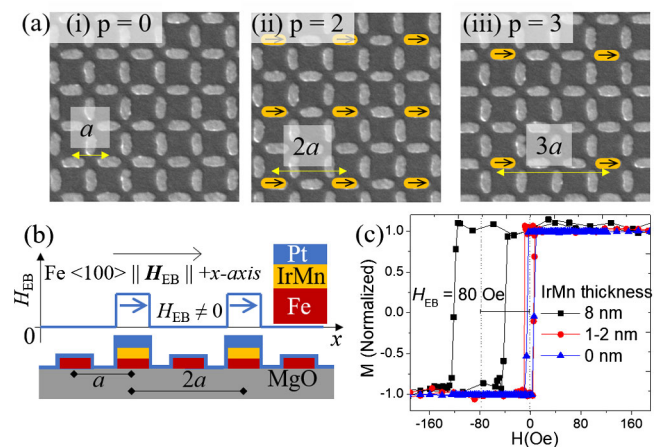


FIG. 1. (a) SEM images of (i) ASI ($a = 400$ nm), (ii) h_{2a} -ASI, and (iii) h_{3a} -ASI. The exchange-biased sites are highlighted, and its direction indicated by arrows. The device edge is aligned to the direction of H_{EB} which is along Fe $\langle 100 \rangle$ crystallographic axis. (b) Schematic cross section of x sublattice and the local field due to H_{EB} as a function of position in h_{2a} -ASI. (c) Hysteresis loop of Fe (7 nm) film with IrMn layer of different thicknesses measured using longitudinal magneto-optic Kerr effect. 8 nm of IrMn imparts an H_{EB} of 80 Oe. H_{EB} is almost nonexistent when IrMn layer is thinned down to around 1–2 nm by ion milling.

this a *hybrid* square artificial spin ice (h_{pa} -ASI) as it is a composite of nonidentical nanomagnets (90 nm wide and 240 nm long) with uniaxial [Fe(7 nm)] and unidirectional [Fe(7 nm)/IrMn(8 nm)] anisotropy. This breaks the spin reversal symmetry, effectively pinning the magnetization of a nanoelement along the direction of the exchange bias. Here, the low energy configurations minimize dipolar interactions with neighboring spins subject to satisfying the local exchange bias.

The most striking consequence of this localized exchange bias is on the low energy states of h_{pa} -ASI obtained after demagnetization. Here, the resulting magnetic configurations depend strongly on the periodicity p of the pinning. Approximating the islands as point dipoles, the total energy of a spin at site i in the h_{pa} -ASI is

$$E_{\text{tot}}^i = D \sum_j s_i s_j \frac{\hat{\boldsymbol{\sigma}}_i \cdot \hat{\boldsymbol{\sigma}}_j - 3(\hat{\boldsymbol{\sigma}}_i \cdot \hat{\boldsymbol{r}}_{ij})(\hat{\boldsymbol{\sigma}}_j \cdot \hat{\boldsymbol{r}}_{ij})}{|\hat{\boldsymbol{r}}_{ij}|^3} + E_{\text{ani}}^i + s_i \hat{\boldsymbol{\sigma}}_i \cdot \mathbf{H}_{\text{ext}}^i + s_i \hat{\boldsymbol{\sigma}}_i^x \cdot \mathbf{H}_{\text{EB}}^i.$$

The first term on the right hand side is the total magnetostatic energy of the spin at site i with orientation parallel to unit vector $\hat{\boldsymbol{\sigma}}_i$, polarity $s_i \in \{-1, 1\}$ and a dipolar coupling to other moments of strength determined by $D = \mu_o(M_S V)^2/4\pi a^3$ (M_S : saturation magnetization and V : volume of nanomagnet). The second term is the anisotropy energy of the nanomagnet; the third term is the Zeeman energy due to the external magnetic field; and the fourth term—which applies only if the spin is pinned—is the Zeeman energy resulting from the coupling to the exchange-bias field aligned along the x axis with a magnitude H_{EB} .

Our fabricated arrays are too thick to be thermally active within experimental limits. Furthermore, annealing can destroy the interfacial exchange bias. Hence, we used a field demagnetization protocol to probe the low energy states. By selecting large magnitudes of $H_{\text{EB}} \sim 80$ Oe [Fig. 1(c)], we arrest the magnetization of a pinned spin and thus heavily constrain its reversal dynamics. Varying the periodicity ($p = 1$ to 16) of the local field allows one to adjust the density of constrained spins: a small p means dense pinning; a high p means less dense pinning. In what follows, we show that varying the pinning density in h_{pa} -ASI controls equilibration processes and gives insight into quenched disorder. We first consider the effect of introducing a single pinned spin into a regular square lattice and show that this leads to local control over relaxation timescales and correlations. The simulated results correspond well to the observed experimental results of the alternating field demagnetization protocol with even and odd exchange-bias pinning period. Finally, simulated thermal annealing results show that this hybrid system effectively tunes the ordering processes.

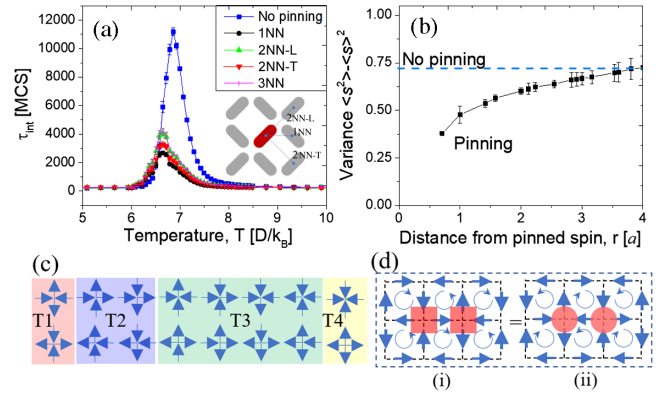


FIG. 2. (a) The integrated correlation time (τ_{int}) shows a peak in each case at the critical temperature; however, this is greatly suppressed by the presence of a nearby pinning site. The inset is a schematic showing three classes of nearest neighbors in ASI: first nearest neighbors (1NN), second nearest neighbors located in the same vertex (2NN- L), and second nearest neighbors which span adjacent vertices (2NN- T). Central spin is shown in red. (b) The variance of the s_i (t) as a function of distance from a pinned spin. The dashed line denotes variance in case of no pinning. In both cases, the variance is evaluated at the critical temperature. (c) Four vertex types in square ASI with different spin topologies. (d) Two (i) and (ii) degenerate GSs/T1 phase domains of square ASI. We present these two phase domains using square and round symbols throughout.

In the simplest approximation, a pinned spin is assumed always to align with its H_{EB} and change the local energy landscape by acting as a source of an effective “bias” dipolar field on nearby spins. As described in the Supplemental Material [32], Monte Carlo simulations were used to estimate the integrated correlation time of spins with and without pinned neighbors as a function of temperature. Previous work on spin ice has demonstrated that these Monte Carlo timescales match well with experimentally measured relaxation times [35]. Example results are shown in Fig. 2(a). In each case, a peak is observed as the transition temperature is crossed, consistent with the effects of critical slowing down. However, this peak is suppressed for spins close to the pinning site, in most cases by $\sim 60\%$. Correlations are studied in Fig. 2(b) where the variance, $\langle s_i^2 \rangle - \langle s_i \rangle^2$, is shown as a function of radial distance r from the pinning site. The data for the pinned system intersects the uniform value one finds for an unpinned system at $r \sim 4a$ [equivalently, the 17th nearest neighbor (NN)]. This example shows the long-range effects that arise through the pinning of even a single spin. It should be noted that vertex ordering is usually (but not always) controlled by the dominant dipolar interaction between the first nearest neighbors (1 nn); however, this falls off rapidly with distance and may be supplanted by next nearest neighbor interactions (see Supplemental Material [32]).

We now compare this prediction—that large, long-range correlations arise from pinning—with the experimental

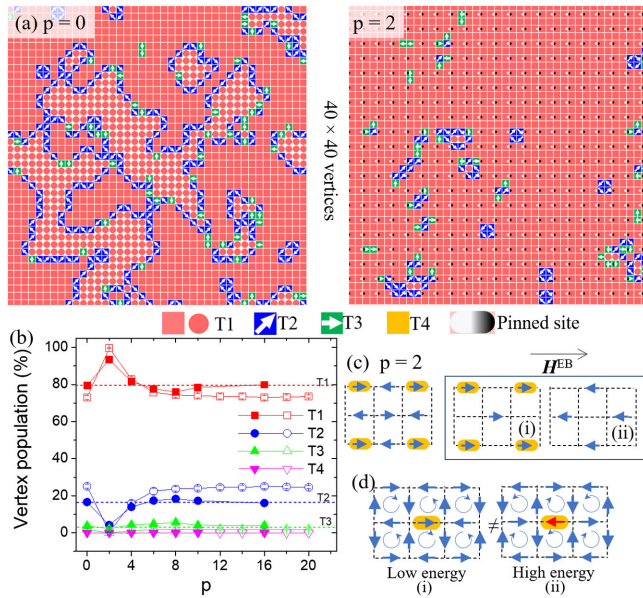


FIG. 3. (a) Vertex map and (b) population statistics of demagnetized h_{pa} -ASI ($p = 0$ and 2). Vertices $T1$, $T2$, $T3$, and $T4$ are color coded in red, blue, green, and yellow, respectively. Arrows indicate direction of the net moment of a vertex and the pinned spins are indicated by black-white blocks. In (b) filled and open symbols represent results of experiments and simulations, respectively. (c) Schematic of one of the antiferromagnet order in the x sublattice of h_{2a} -ASI with pinned sites highlighted in yellow. The bipartite lattices (i) and (ii) of the antiferromagnet order are indicated. All the pinned sites appear only in bipartite lattice (i). The bipartite lattice (ii) has no pinning centers. (d) Schematic shows the two $T1$ orderings (i) and (ii). Exchange bias at the site highlighted prefers (i) over (ii). The $T1$ domain (ii) with moment antiparallel to exchange bias (red arrow) has higher energy.

results of an alternating field demagnetization applied to samples of various pinning densities. While not thermally active at room temperature, fluctuations near to the coercive field will reflect the influence of pinned spins. Experimental results are compared to simulated configurations achieved with a similar alternating field protocol (discussed in Supplemental Material [32]).

The results shown below are in terms of vertex type [square ASI has four vertex types, see Fig. 2(c)]. The ground state (GS) for h_{0a} -ASI is constituted by tiling alternately the two $T1$ vertices. This results in a twofold degenerate GSs [schematic (i) and (ii) of Fig. 2(d)]. Only a thermal demagnetization has so far been able to access these GSs [36–38], while a field demagnetization always results in multiple $T1$ domains separated by higher energy $T2/T3$ domain walls [vertex map of Fig. 3(a)] [39–41].

The simplest even pinning case, h_{2a} -ASI, involves exchange bias applied at alternating sites of the x sublattice, as sketched in Fig. 1(a). This breaks the degeneracy of the two GSs resulting in a unique $T1$ GS. Experimental results confirm that a field demagnetization protocol can attain this

$T1$ phase domain throughout more than 90% of the array [Figs. 3(a) and 3(b)]. This result is comparable to what can be achieved with a thermally demagnetized square ASI [36–38].

Consider the x sublattice of the h_{2a} -ASI with a $T1$ ordered state [see Fig. 3(c)]. The spin arrangement can be viewed as a *bipartite* lattice of a *Néel* antiferromagnet with two interpenetrating but antiparallel spin lattices [(i) and (ii) of Fig. 3(c)]. During demagnetization, as the amplitude of the applied square wave is reduced, the moments with the largest barrier freeze first. In the case of h_{pa} -ASI, those moments which are pinned freeze first along H_{EB} . As discussed above, these frozen spins bias their neighbors into configurations of minimum magnetostatic energy. The result is a $T1$ ordered state (i) as shown in Fig. 3(d) for a specific pinning site. Thus, the pinned spins act as *nucleation sites* for the GS. For even pinning periodicity, low energy $T1$ domains nucleate around each of these pinned sites. The domains are all *in phase* and grow together coherently, merging and removing any separating $T2$ domain walls. In this way a large area of $T1$ ordering is obtained by demagnetization. However, we also observe different elementary excitations above this antiferromagnetic order such as closed loops of $T2$ vertices, $T3$ pairs, and short strings of $T2$ with $T3$ terminations that are signatures of thermal annealing process as reported by Jason *et al.* [37]. These may be attributed to quenched disorder in the array.

With $p = 4$ and 6 , $T1$ domains of opposite phase start to appear in regions between the pinned sites with fewer elementary excitations (see Supplemental Material [32]). This is expected from our simple model: the influence of a pinned spin extends to a distance of around $4a$. Beyond this, we would expect those regions to behave more like unpinned square ice in which the usual quenched disorder acts as nucleation sites. Clearly, when the $T1$ domains around such quenched disorder region are out-of-phase, then $T2$ domain walls are formed between the regions, as clearly shown for the case of h_{4a} -ASI and h_{6a} -ASI. Indeed, for $p \geq 8$, the pinned sites are far enough away that their effects become indistinguishable from any random quenched disorder and hence the system behaves similarly to ASI without pinning (reflected also in the vertex population statistics). The vertex statistics [Fig. 3(b)] and vertex maps of h_{pa} -ASI are reproduced well in simulated field demagnetization (discussed further in Supplemental Material, Sec. IV. II [32]).

Arrays with odd pinning exhibit distinct features as shown by MFM images and the vertex statistics given in Figs. 4(a) and 4(b), respectively. The highly constrained h_{1a} -ASI exhibits a $T2$ dominated vertex array with short zigzag stripe domains of $T2$ [shown by cyan color in Fig. 4(a)]. This is expected as the islands in one entire sublattice are pinned. Considering just spins in the other free sublattice (y sublattice), the $2NN-L$ interaction promotes chains of ferromagnetically ordered islands, while the $2NN-T$ interaction

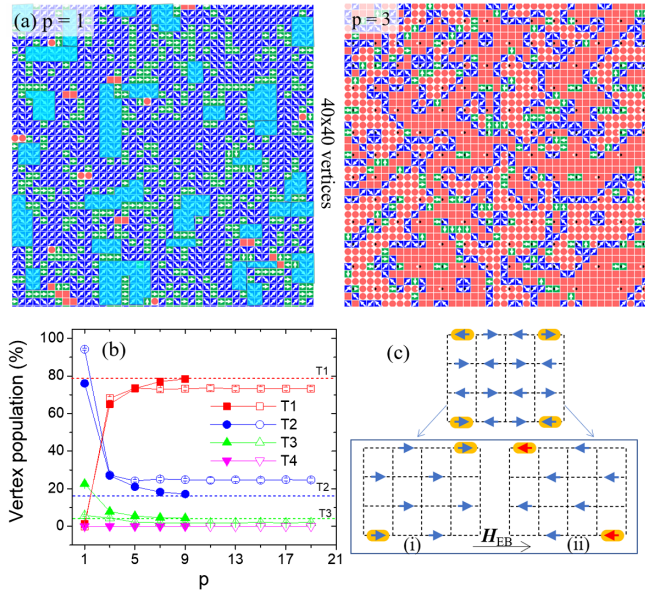


FIG. 4. (a) The vertex maps of field demagnetized h_{pa} -ASI with odd p values ($=1, 3$). The zigzag phase in h_{1a} -ASI is highlighted in cyan (b) vertex statistics of h_{pa} -ASI with odd p values. Filled and open symbols represent results of experiments and simulations, respectively. (c) Schematic of one of the antiferromagnet order in the x sublattice of h_{3a} -ASI with pinned sites highlighted in yellow. The bipartite lattices (i) and (ii) of the antiferromagnet order are indicated. Pinned sites appear in both Néel bipartite sublattices (i) and (ii), as shown. The bipartite sublattice (i) has all the spins aligned parallel to exchange bias but the (ii) has spins antiparallel to exchange bias (red arrows). Thus, a simple antiferromagnetic Néel ordering cannot simultaneously minimize both exchange-bias energy and dipolar energy in case of h_{3a} -ASI.

ensures that these chains are arranged antiparallel. A zigzag $T2$ ordered state then appears in a manner similar to results found in [29]. In this way, pinning results in system in which the dominant *free* interaction is that between second nearest neighbors.

In the case of h_{3a} -ASI, the $T1$ domains nucleated at adjacent pinning sites are out of phase. This leads to $T2/T3$ domain walls separating multiple $T1$ phase domains. Figure 4(c) contains a schematic of this pinning overlaid on the x sublattice with spins ordering in one of the $T1$ domains. In this case, the pinning sites in each of the Néel bipartite sublattices will create out-of-phase antiferromagnetic domains. The h_{3a} -ASI exhibits complex vertex arrangements consisting of an intricate network of $T2$ domain walls along with a large number of higher energy isolated $T3$ pairs [Fig. 4(a)]. It is observed that in some cases $T1$ domains nucleate and grow from certain pinned sites while in other cases the $T1$ domains are suppressed and instead $T3$ pairs are created. Simulations suggest that in this case a demagnetization process is unable to create long-range ordering (Supplemental Material [32], Sec. IV).

As the pinning period is increased, in h_{5a} -ASI the density of the $T2$ domain wall drops and the size of the

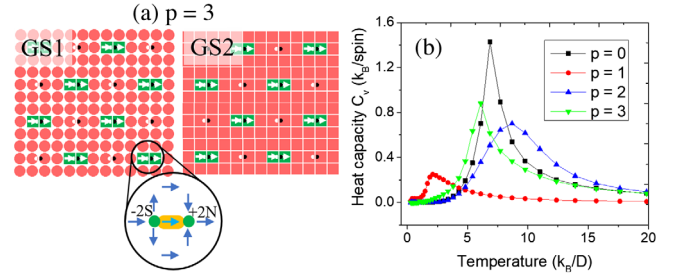


FIG. 5. (a) Ground states (GS1 and GS2, with pinning sites indicated) vertex maps of h_{3a} -ASI obtained in Monte Carlo simulations. (b) Heat capacities for no pinning $p = 0$ and $p = 1, 2, 3$. Even (odd) pinning raises (lowers) the critical temperature.

$T1$ domain increases allowing reduction of the magneto-static energy. In h_{7a} -ASI and h_{9a} -ASI, the vertex populations [Fig. 4(b)] and maps converge to those of a regular ASI as seen in both experiment and simulation.

In short, the consequences of induced correlations are especially clear for the highest pinning densities ($p = 1$ or 2). Varying the pinning periodicity thus allows for engineering vertex populations, and through this, offers control over the resultant global magnetic texture of an array.

As noted, the experimental behavior of h_{pa} -ASI is reproduced well in field demagnetization simulations. In order to examine the development of long-range ordering, thermal annealing Monte Carlo was used to probe the possible GSs. Interestingly, h_{3a} -ASI exhibits a GS with twofold degeneracy comprising a majority of $T1$ ordering with $T3$ pairs at alternating pinning sites [Fig. 5(a)]. During the transition from disordered paramagnetic phase to an ordered phase, the system spontaneously adopts one GS over the other. The $T3$ pairs—composed of adjacent $2N/2S$ vertices—satisfy the pinning constraint. Also, the dipolar energy required to create complex network of $T2$ domain walls across the array is larger than that required to keep these $T3$ pairs in the background $T1$ ordered state.

The heat capacity of different h_{pa} -ASI calculated shows peaks corresponding to the phase transition to the ordered phase. For h_{0a} -ASI, this peak occurs at $T_c \approx 7.2 D/k_B$ [Fig. 5(b)] in agreement with [42,43]. Even pinning increases the T_c while odd pinning lowers it. The behavior of h_{2a} -ASI can be understood from the fact that the pinned spins at even sites are causing $T1$ phase domain to freeze around it at higher temperatures, thus reinforcing nucleation of GSs at higher temperatures which in turn increases the critical temperature. For the odd period of $p = 1$, a transition from paramagnetic to zigzag (ferromagnetic) phase is observed at a much lower temperature. This is due to the reduced coupling strength as the dominant second nearest neighbor interactions here is weaker than that of the first nearest neighbor interaction [43]. A similar logic also holds for $p = 3$. Here, the regular $T1$ order is rather disrupted by the $T3$ pairs. Fluctuations are present to lower temperatures.

In this way, *local* pinning allows for control of *global* critical quantities.

We have demonstrated how a hybrid artificial magnetic system made of nanomagnets of uniaxial and site-specific unidirectional anisotropy exhibits different magnetic textures according to a controlled periodicity p , thus allowing for a degree of configurability. Exchange bias is applied at local sites of a square ASI. This, in turn, narrows the dynamics in the configurational phase space and enables control over its GS configuration. This local pinning offers a route to controlling correlations within arrays, allowing for the engineering of vertex populations. As a corollary, we show that the conventional GS of square ASI can be achieved based on a field protocol *alone* for $p = 2$ —in effect, thermal demagnetization without a thermal bath. Monte Carlo results of thermal annealing of this system show that this hybrid system allows for fine-scale tuning of ordering processes. A variety of magnetic textures is observed: from a zigzag ferromagnetic phase ($p = 1$) to complete $T1$ ordering attainable just through an external field protocol ($p = 2$) to an unconventional GS with $T3$ excited pairs embedded in the antiferromagnetic $T1$ phase ($p = 3$). The pinning fields then act as “artificial quenched disorder” which drive differences in vertex populations.

A natural extension to the present work will be to create thermally active h_{pa} -ASI where the pinned sites remain frozen in predetermined magnetization states while the remaining array is dynamic. This will allow the investigation of energy minimization dynamics, controlled creation of magnetic monopoles and its dynamics, phase transitions in the presence of periodic pinning, and further extend it to thermally driven nanomagnetic computing devices.

This work was supported by the National Science Foundation Grant No. NSF/DMR 1604186. Part of this work was conducted at the Washington Nanofabrication Facility / Molecular Analysis Facility, a National Nanotechnology Coordinated Infrastructure (NNCI) site at the University of Washington, which is supported in part by funds from the Molecular Engineering & Sciences Institute, the Clean Energy Institute, the Washington Research Foundation, the M. J. Murdock Charitable Trust, the National Science Foundation, and the National Institutes of Health. G. M. M. was supported by the Carnegie Trust for the Universities of Scotland, and the Universities of Glasgow and Manitoba. R. L. S. acknowledges the support of the Natural Sciences and Engineering Research Council of Canada (NSERC)—R. L. S. received financial support from the Conseil de recherches en sciences naturelles et en génie du Canada (CRSNG).

*kannanmk@uw.edu

- [1] R. F. Wang, C. Nisoli, R. S. Freitas, J. Li, W. Mcconville, B. J. Cooley, M. S. Lund, N. Samarth, C. Leighton, V. H. Crespi, and P. Schiffer, *Nature (London)* **439**, 303 (2006).
- [2] R. Moessner and A. P. Ramirez, *Phys. Today* **59**, No. 2, 24 (2006).
- [3] C. Nisoli, R. Moessner, and P. Schiffer, *Rev. Mod. Phys.* **85**, 1473 (2013).
- [4] A. P. Ramirez, *Annu. Rev. Mater. Sci.* **24**, 453 (1994).
- [5] M. J. Harris, S. T. Bramwell, D. F. McMorrow, T. Zeiske, and K. W. Godfrey, *Phys. Rev. Lett.* **79**, 2554 (1997).
- [6] S. T. Bramwell and M. J. P. Gingras, *Science* **294**, 1495 (2001).
- [7] M. J. Morrison, T. R. Nelson, and C. Nisoli, *New J. Phys.* **15**, 045009 (2013).
- [8] C. Nisoli, V. Kapaklis, and P. Schiffer, *Nat. Phys.* **13**, 200 (2017).
- [9] J. Sklenar, Y. Lao, A. Albrecht, J. D. Watts, C. Nisoli, G.-W. Chern, and P. Schiffer, *Nat. Phys.* **15**, 191 (2019).
- [10] I. Gilbert, Y. Lao, I. Carrasquillo, L. O’Brien, J. D. Watts, M. Manno, C. Leighton, A. Scholl, C. Nisoli, and P. Schiffer, *Nat. Phys.* **12**, 162 (2016).
- [11] L. J. Heyderman and R. L. Stamps, *J. Phys. Condens. Matter* **25**, 363201 (2013).
- [12] N. Rougemaille and B. Canals, *Eur. Phys. J. B* **92**, 62 (2019).
- [13] C. H. Marrows, [arXiv:1611.00744](https://arxiv.org/abs/1611.00744).
- [14] E. Mengotti, L. J. Heyderman, A. F. Rodríguez, F. Nolting, R. V. Hügli, and H. Braun, *Nat. Phys.* **7**, 68 (2011).
- [15] Y. Perrin, B. Canals, and N. Rougemaille, *Nature (London)* **540**, 410 (2016).
- [16] R. C. Silva, R. J. C. Lopes, L. A. S. Mol, W. A. Moura-Melo, G. M. Wysin, and A. R. Pereira, *Phys. Rev. B* **87**, 014414 (2013).
- [17] S. Gliga, G. Hrkac, C. Donnelly, J. Büchi, A. Kleibert, J. Cui, A. Farhan, E. Kirk, R. V. Chopdekar, Y. Masaki, N. S. Bingham, A. Scholl, R. L. Stamps, and L. J. Heyderman, *Nat. Mater.* **16**, 1106 (2017).
- [18] I. Gilbert, G. W. Chern, S. Zhang, L. O’Brien, B. Fore, C. Nisoli, and P. Schiffer, *Nat. Phys.* **10**, 670 (2014).
- [19] J. Lehmann, C. Donnelly, P. M. Derlet, L. J. Heyderman, and M. Fiebig, *Nat. Nanotechnol.* **14**, 141 (2019).
- [20] Y.-L. Wang, Z.-L. Xiao, A. Snezhko, J. Xu, L. E. Ocola, R. Divan, J. E. Pearson, G. W. Crabtree, and W.-K. Kwok, *Science* **352**, 962 (2016).
- [21] H. Arava, P. M. Derlet, J. Vijayakumar, J. Cui, N. S. Bingham, A. Kleibert, and Laura J. Heyderman, *Nanotechnology* **29**, 265205 (2018).
- [22] P. Gypens, J. Leliaert, and B. Van Waeyenberge, *Phys. Rev. Applied* **9**, 034004 (2018).
- [23] Y. Qi, T. Brintlinger, and J. Cumings, *Phys. Rev. B* **77**, 094418 (2008).
- [24] D. Shi, Z. Budrikis, A. Stein, S. A. Morley, P. D. Olmsted, G. Burnell, and C. H. Marrows, *Nat. Phys.* **14**, 309 (2018).
- [25] M. Saccone, K. Hofhuis, Y.-L. Huang, S. Dhuey, Z. Chen, A. Scholl, R. V. Chopdekar, S. van Dijken, and A. Farhan, *Phys. Rev. Mater.* **3**, 104402 (2019).
- [26] A. Farhan, C. F. Petersen, S. Dhuey, L. Anghinolfi, Q. H. Qin, M. Saccone, S. Velten, C. Wuth, S. Gliga, P. Mellado, M. J. Alava, A. Scholl, and S. Van Dijken, *Nat. Commun.* **8**, 995 (2017).
- [27] E. Mengotti, L. J. Heyderman, A. Fraile Rodriguez, A. Bisig, L. Le Guyader, F. Nolting, and H. B. Braun, *Phys. Rev. B* **78**, 144402 (2008).

- [28] R. V. Chopdekar, G. Duff, R. V. Hügli, E. Mengotti, D. A. Zanin, L. J. Heyderman, and H. B. Braun, *New J. Phys.* **15**, 125033 (2013).
- [29] V. M. Parakkat, K. Xie, and K. M. Krishnan, *Phys. Rev. B* **99**, 054429 (2019).
- [30] J. Nogués and I. K. Schuller, *J. Magn. Magn. Mater.* **192**, 203 (1999).
- [31] R. L. Stamps, *J. Phys. D* **33**, R247 (2000).
- [32] See Supplemental Material at <http://link.aps.org/supplemental/10.1103/PhysRevLett.126.017203> for additional information, which includes Refs. [33,34].
- [33] G. W. Chern, C. Reichhardt, and C. J. Olson Reichhardt, *New J. Phys.* **16**, 063051 (2014).
- [34] B. Yucesoy, J. Machta, and H. G. Katzgraber, *Phys. Rev. E* **87**, 012104 (2013).
- [35] L. D. C. Jaubert and P. C. W. Holdsworth, *Nat. Phys.* **5**, 258 (2009).
- [36] A. Farhan, P. M. Derlet, A. Kleibert, A. Balan, R. V. Chopdekar, M. Wyss, J. Perron, A. Scholl, F. Nolting, and L. J. Heyderman, *Phys. Rev. Lett.* **111**, 057204 (2013).
- [37] J. P. Morgan, A. Stein, S. Langridge, and C. H. Marrows, *Nat. Phys.* **7**, 75 (2011).
- [38] X. M. Chen, B. Farmer, J. S. Woods, S. Dhuey, W. Hu, C. Mazzoli, S. B. Wilkins, R. V. Chopdekar, A. Scholl, I. K. Robinson, L. E. De Long, S. Roy, and J. T. Hastings, *Phys. Rev. Lett.* **123**, 197202 (2019).
- [39] Z. Budrikis, P. Politi, and R. L. Stamps, *Phys. Rev. Lett.* **107**, 217204 (2011).
- [40] Z. Budrikis, P. Politi, and R. L. Stamps, *J. Appl. Phys.* **111**, 07E109 (2012).
- [41] Z. Budrikis, J. P. Morgan, J. Akerman, A. Stein, P. Politi, S. Langridge, C. H. Marrows, and R. L. Stamps, *Phys. Rev. Lett.* **109**, 037203 (2012).
- [42] R. C. Silva, F. S. Nascimento, L. A. S. Mól, W. A. Moura-Melo, and A. R. Pereira, *New J. Phys.* **14**, 015008 (2012).
- [43] R. Macêdo, G. M. Macauley, F. S. Nascimento, and R. L. Stamps, *Phys. Rev. B* **98**, 014437 (2018).